JACS
JOURNAL OF THE AMERICAN CHEMICAL SOCIETY

ARTICLE

pubs.acs.org/JACS

Ortho-Branched Ladder-Type Oligophenylenes with Two-Dimensionally π-Conjugated Electronic Properties

Hsin-Hau Huang, Ch. Prabhakar, Kuo-Chun Tang, Pi-Tai Chou,* Guan-Jhih Huang, and Jye-Shane Yang*

Department of Chemistry, National Taiwan University, Taipei, 10617 Taiwan

Supporting Information

ABSTRACT: The synthesis, photochemical and electrochemical properties, and electronic structures of a series of star-shaped ladder-type oligophenylenes **S*n*** (n = 7, 10, 13, 16, 19, and 22), including one multibranched case **S19mb**, are reported and compared with the linear para-phenylene ladders **R*n*** (n = 2−5 and 8) and the stepladder analogues **SF*n*** (n = 10, 16, and 22). The n value refers to the number of π-conjugated phenylene rings. Functionalized isotruxenes are the key synthetic building blocks, and **S22** is the largest monodispersed ladder-type oligophenylene known to date. The **S*n*** systems possess the structural rigidity of **R*n*** and the ortho−para phenylene connectivity of **SF*n***. Consequently, **S*n*** represents the first class of branched chromophores with fully two-dimensional conjugation in both ground- and excited-state configurations. Evidences include the excellent linear correlations for the optical 0−0 energies or the first oxidation potentials of **S*n*** and **R*n*** against the reciprocal of their n values, delocalized HOMO and LUMO based on density functional theory calculations, and molecule-like fluorescence anisotropy. The resulting model of effective conjugation plane (ECP) for the two-dimensional π-conjugated systems compliments the concept of effective conjugation length (ECL) for one-dimensional oligomeric systems. Other implications of the observed structure−property relationships are also included.

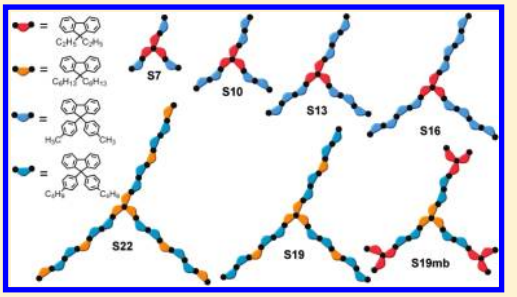

INTRODUCTION

Monodispersed conjugated oligomers (MCO) constitute an important class of organic electronic materials.[1−15] They possess the merits of molecule-like structural purity and polymer-like flexibility, thermal stability, and film-forming properties. Many recent efforts have been devoted to synthesis of multidimensional MCO such as two-dimensional stars and discs as well as three-dimensional cruciforms and dendrimers.[8−16] The extra dimensions in MCO hold great promise for improved solubility, new film morphology, and/or decreased electronic anisotropy. However, their effective conjugation length (ECL)[17,18] is often poorly defined or confined in a short one-dimensional segment. This stems from the fact that electronic coupling among the branched segments strongly depends on the degree of steric congestion and electronic communications through the branching units. Large torsion angles[3,19] and cross-conjugated linkers (e.g., meta-phenylene)[2,13,14] in the conjugated backbone could severely hamper or even truncate the exciton delocalization. Accordingly, the steric and electronic characters of the branching units play a pivotal role in developing MCO of truly multidimensional electronic conjugation.

Phenylene-based conjugated oligomers[4−10,14−16] and polymers[9,20−23] are promising candidates for organic electronics due to their high photoluminescence quantum efficiency, prominent charge-carrier mobility, and great electrochemical and thermal stability. The ring-bridging approach that connects adjacent phenylene rings at the ortho positions with solubilizer-substituted saturated carbons can simultaneously enhance their solubility and conformational planarity and rigidity. The so-called stepladder and ladder-type polyphenylenes correspond to the partly and fully bridged systems, respectively. Recently, an intriguing position effect of ring-bridging was observed for indenofluorenes (**1**, R = H), where the *anti*-isomer **1a** displays red-shifted absorption and fluorescence maxima (12−13 nm) with respect to the *syn*-isomer **1s**.[24] While this position effect reflects the differences in linearity of the phenylene backbone (**1a** > **1s**) or the pattern of substitutions (para in **1a** vs ortho in **1s**), the role of this position effect in a larger ladder system remains to be evaluated.

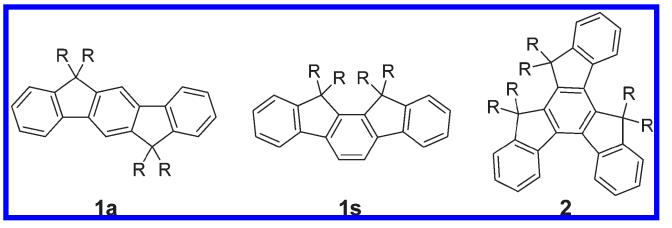

An extension of the one-dimensional **1s** by adding another indeno group to the central ring leads to the two-dimensional isotruxene **2** with an ortho−para phenylene connectivity. We have shown that **2** is a branching unit that allows strong electronic coupling between the ortho and the para branches.[15] A combination of ladder-type para-phenylene segments and

Received: March 9, 2011
Published: April 28, 2011

dx.doi.org/10.1021/ja202144v | J. Am. Chem. Soc. 2011, 133, 8028–8039

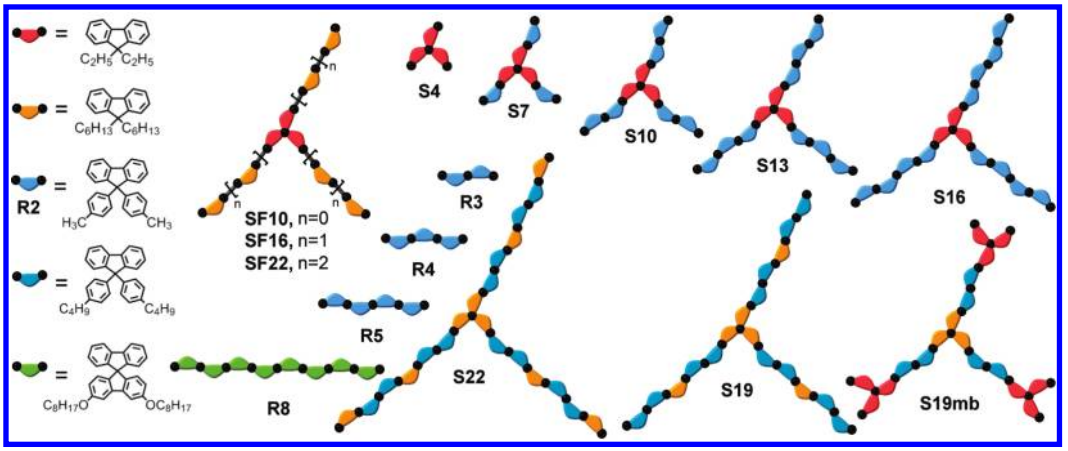

Figure 1. Schematic representation of the structures of oligophenylenes **S*n***, **R*n***, and **SF*n***, where the black dots represent the backbone phenylene rings with a number of *n*. The difference in colors between the black dots represents the difference of solubilizing substituents on the saturated carbons. See Supporting Information Charts S1−S4 for chemical structures of **S*n***.

2 should lead to systems fulfilling the needs for two-dimensional conjugation. Indeed, we recently communicated[16] the first example of fully conjugated stars with the isotruxene-derived ladder-type oligophenylenes **S*n***, where **S** and ***n*** denote the shape (i.e., *s*tar) of the structure and the total number (i.e., 4, 7, 10, 13, and 16) of phenylene rings in the π-conjugated backbone, respectively (Figure 1). The extra dimension added by the ortho branch in **S*n*** elongates the ECL and lowers the energy gap, leading to red-shifted fluorescence for **S16** vs a linear long-chain ladder polymer[21] (470 nm vs 464 nm). Unlike the ECL of ~12 phenylene rings for one-dimensional ladders (**R*n***),[22] the absence of saturation in the emission wavelength of **S16** led us to extend the concept of ECL to a two-dimensional cyclic region that defines the boundary of exciton delocalization in **S*n***. We will call it effective conjugation plane (ECP) hereafter.

Several important questions remained open in the study of **S*n***. First, we have proposed[16] that ECP is a cyclic extension of ECL: namely, the diameter of ECP for **S*n*** equals the ECL for the linear ladder **R*n***. This in turn suggests that saturation in electronic transition energy for the **S*n*** series will occur at the size of **S19** or **S22**. However, this prediction is not yet verified, because previous attempts to prepare **S*n*** larger than **S16** with the same solubilizers were unsuccessful. Second, despite the presence of effective two-dimensional conjugation in **S*n*** containing one ortho branch, it is unknown if the same phenomenon is also present in systems of multiple ortho branches. This is another crucial point for establishing the ECP model. Third, neither the general picture of electronic structure nor the origins of allowed transitions in the absorption spectra of **S*n*** are fully characterized.

In the present work, we address all these questions. Two larger systems **S19** and **S22** and one *m*ulti-*b*ranched system **S19mb** containing four ortho branching cores have been successfully prepared by changing the solubilizers and/or the synthetic strategy. In addition, DFT and TD-DFT calculations and fluorescence anisotropy measurements on **S*n*** have been conducted to characterize their electronic structures. Our results confirm the proposed ECP model and show that ortho-conjugation is as effective as para-conjugation provided that the planarity and rigidity of the π-conjugated backbone is sufficiently high. The backbone planarity is more important than the position of bridging atoms in determining the optical properties of these ladder-type oligomers. The electronic character of these branched oligophenylenes is molecule-like rather than polymer-like in terms of the single-chromophore and two-dimensional optical transition behavior.

RESULTS AND DISCUSSION

Synthesis. The synthesis of **S7**, **S10**, **S13**, **S16**, and **S19mb** adopted a convergent synthetic strategy by linking an isotruxene core and three corresponding arms. The synthetic details for the former four compounds have been communicated,[16] and the strategy for **S19mb** is illustrated in Scheme 1. The Suzuki-Miyaura cross coupling of the boronic acid functionalized isotruxene core **S4′BA** and the bromo and ester functionalized 5-phenylene branched arm **A5bBr** formed the ester-containing 19-phenylene precursor ***pre*-S19mb**. The subsequent nucleophilic carbonyl addition and intramolecular Friedel−Crafts alkylation reactions afforded the fully ring-bridged ladder scaffold of **S19mb**. Both the reactants **S4′BA** and **A5bBr** contain the isotruxene moieties and can be prepared from the parent isotruxene and isotruxene monobromide **ITBr**, respectively. We have developed facile synthetic methods for the parent isotruxene (i.e., **2** with R = H).[25] We also showed that they can be modified to form prefunctionalized isotruxenes with functional groups at selected phenylene ring(s).[26] The synthesis of **ITBr** provided a new example (Supporting Information [SI]). Scheme 2 shows the conversion of **ITBr** to **A5bBr**. Base-promoted alkylations of **ITBr** were conducted with *t*-BuOK in the presence of catalytic amounts of 18-crown-6. The resulting **S4Br** was converted to boronic ester **S4BE** by the Miyaura boration reaction and then to **A5bBr** by the Suzuki coupling with the ring-bridging precursor diethyl 2,5-dibromobenzene-1, 4-dioate (***pre*-RB**). The reactant **S4′BA** was prepared by following the previously reported method[16] for its analogue **S4BA**. In brief, the synthesis was accomplished in three steps starting with the parent isotruxene: namely, alkylations on the saturated carbons, brominations on the terminal phenylenes, and bromo-to-boronic acid transformation. The difference between **S4′BA** and **S4BA** is the length of the alkyl substituents (hexyl vs ethyl) on the saturated carbons. Hexyl chains are no doubt better solubilizers than ethyl chains for a polymer system. However, we have adopted the short-chain isotruxene building blocks **S4Br** and **S4BA** in our previous synthesis of star-shaped isotruxene

dx.doi.org/10.1021/ja202144v |*J. Am. Chem. Soc.* 2011, 133, 8028–8039

Scheme 1

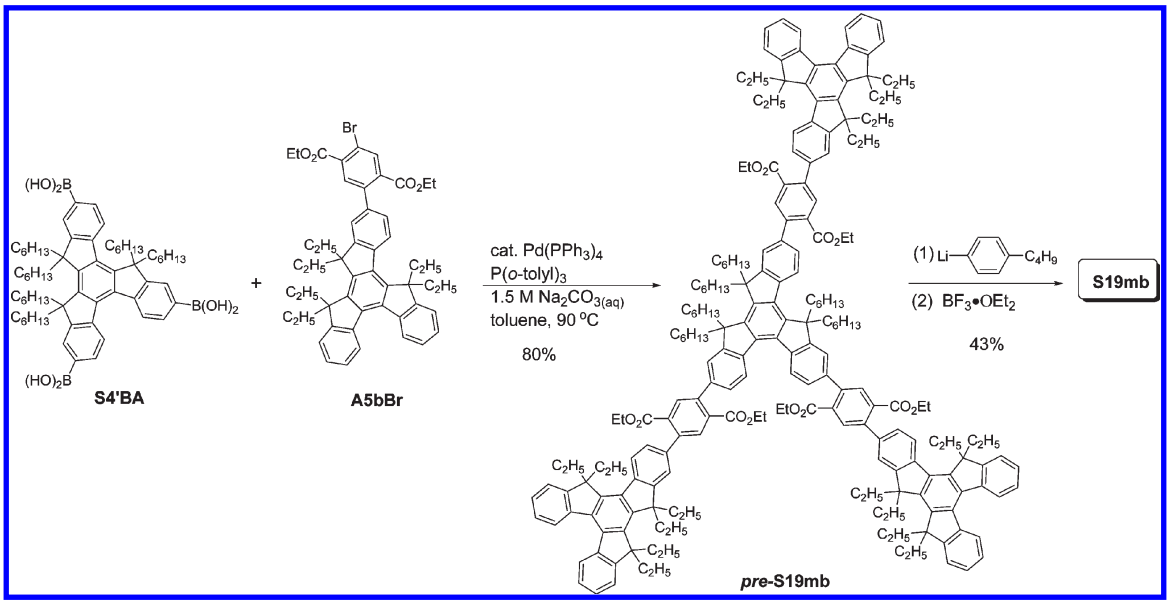

Scheme 2

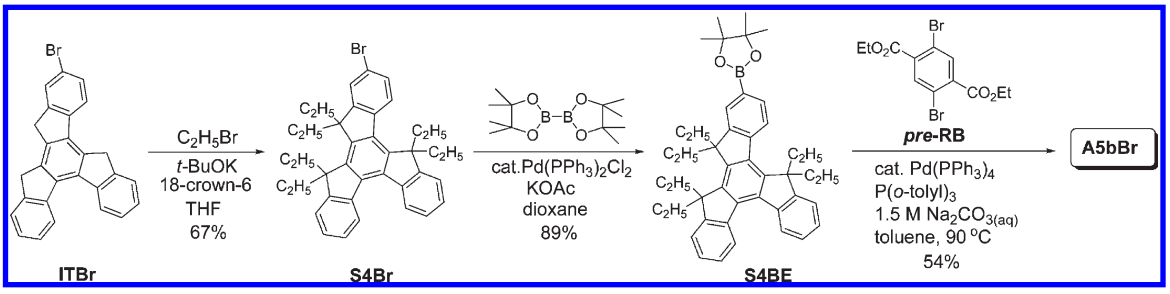

derivatives, including **S7**, **S10**, **S13**, and **S16**. These isotruxene derivatives possess sufficiently good solubility in organic solvents, presumably due to their unsymmetrical structures. A particular reason for using ethyl instead of hexyl groups at the first onset is that the hexyl substituted **S4′** (i.e., **2** with R = C_6H_{13}) is an oily liquid, but the ethyl substituted **S4** (i.e., **2** with R = C_2H_5) is a solid at room temperature. The latter has the advantages of facile compound purification, storage, and transfer. However, the use of ethyl solubilizers has met its limitation in preparing the larger **S*n*** systems **S19** and **S22**. We thus adopted **S4′BA** for the synthesis of **S19** and **S22** as well as **S19mb** in this work.

The synthesis of **S19** and **S22** was accomplished by a mixed convergent and divergent method, which is represented by the case of **S22** (Scheme 3). It is divergent because the entire phenylene backbone was constructed through two stages. The first stage is the Suzuki-Miyaura cross coupling of **S4′BA** and the TMS group-protected 3-phenylene arm **A3TMSBr** that forms the 13-phenylene intermediate ***pre*-S13TMS** bearing a TMS group at each terminal phenylene. The TMS groups were then replaced by iodine atoms with iodine monochloride. The resulting ***pre*-S13I** was then subjected to the second-staged cross coupling reactions with the boronic ester-incorporated 3-phenylene arm **A3BE** to afford the 22-phenylene precursor ***pre*-S22**. The final step of ring-bridging reaction to form **S22** is the same as that for **S19mb**. The overall synthesis is also convergent because not only the above-mentioned reactant **S4′BA** but also **A3TMSBr** and **A3BE** requires multistep syntheses. The synthesis of **A3TMSBr** is shown in Scheme 4. Treatment of 2,7-dibromo-9,9-dihexylfluorene (**FBr_2**) with 1 equiv of *n*-BuLi followed by reaction with chlorotrimethylsilane gave compound **FTMSBr**. After the bromo-to-boronic acid transformation, the resulting **FTMSBA** was subjected to the Suzuki-Miyaura coupling reaction with ***pre*-RB** in the final step of Scheme 2 to form **A3TMSBr**. The synthesis of **A3BE** also involved the Suzuki-Miyaura coupling reaction and the Miyaura boration reaction with the reaction conditions resembling those in Scheme 2 (see Supporting Information). To the best of our knowledge, **S22** is the largest monodispersed oligophenylene reported to date.

It should be noted that the solubilizers on the ring-bridging saturated carbons in **S19**, **S22**, and **S19mb** are different from those in **S4**, **S7**, **S10**, **S13**, and **S16** not only in the central isotruxene core but also in the arms. Such differences are represented with different colors in the represented structures schematically depicted in Figure 1. Unlike the ethyl and *p*-tolyl substituents in the smaller **S*n*** systems, the mixed substituents of hexyl and 4-butylphenyl groups are believed to be crucial in promoting the solubility of **S19**, **S22**, and **S19mb**.

dx.doi.org/10.1021/ja202144v |*J. Am. Chem. Soc.* 2011, 133, 8028–8039

Scheme 3

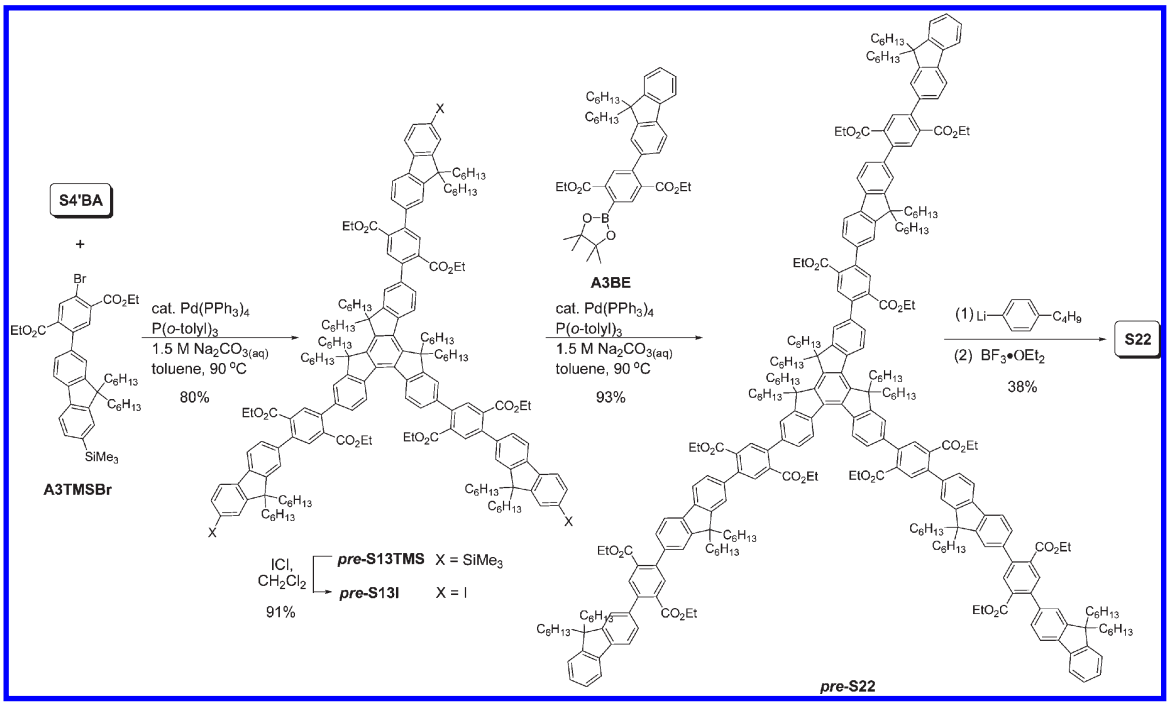

Scheme 4

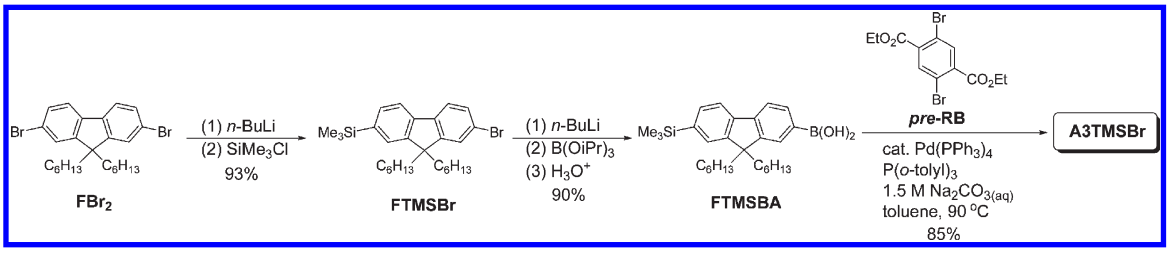

Some of the above reactions might deserve comments, although the reaction conditions are not completely optimized. For the Suzuki coupling reactions, it generally requires higher loading of the Pd catalyst (5−7 mol % per C−Br bond) for substrates containing the isotruxene core to obtain an optimal yield. This situation was also reported for truxene derivatives.[13b] For the two-step ring-bridging reactions for ***pre*-S*n*** → **S*n*** conversion, the yield decreases as the *n* value increases and in the order **S7** (72%) > **S10** (66%) > **S13** (50%) > **S16** (46%) ∼ **S19mb** (43%) > **S22** (38%) ∼ **S19** (35%). The lower yield for larger **S*n*** could be attributed to increased number of reaction sites (i.e., 3, 6, and 12 for **S7**, **S10**−**S16** and **S19mb**, and **S19**−**22**, respectively), decreased solubility of the precursor ***pre*-S*n*** or the alcohol intermediate, and/or increased skeletal branching and solubilizer size (e.g., **S19mb** vs **S16**).

Electronic Properties. The difference in solubilizers among the **S*n*** series should have little or no effects on their electronic properties, because the alkyl and aryl substituents are nearly perpendicular to the phenylene backbone based on the previously communicated X-ray crystal structures of **S4** and **S7**.[16] A support of this argument is from the same electronic spectra recorded for **S4** and **S4′** (not shown). The phenomenon of negligible substituent effects on electronic spectra is also present for the linear ladder **R*n***.[6,7] Therefore, the following discussion on the photochemical and electrochemical properties of **S*n*** will focus on the effect of the phenylene number *n*. In this case, **S19mb** can be considered as a skeletal isomer of **S19**, and the difference between them would reflect the effect of terminal branching. The impact of molecular dimensions will be elucidated by comparing **S*n*** with the linear ladder **R*n*** ($n = 2-5$ and 8).[6,7,16] The effect of molecular planarity and rigidity will be addressed by comparison with our previously reported[15] stepladder systems **SF*n*** ($n = 10$, 16, and 22, Figure 1).

The normalized absorption and fluorescence spectra for **S*n*** in dichloromethane are shown in Figure 2 and the corresponding spectral data are summarized in Table 1. All **S*n***, except for **S4**, display well-defined 0−0 vibronic bands in the absorption spectra and 0−0 and 0−1 bands in the fluorescence spectra. The small Stokes shifts ($\Delta\nu_{st}$) between the absorption and fluorescence 0−0 bands is consistent with the rigid ladder-type structures. Both the absorption and fluorescence spectra undergo bathochromic shift with increasing the number of phenylene rings up to $n = 19$. The small or no difference in the 0−0 wavelengths ($\Delta\lambda \leq 1$ nm) between **S19** and **S22** reveals that the

dx.doi.org/10.1021/ja202144v | J. Am. Chem. Soc. 2011, 133, 8028–8039

effective conjugation size of **S*n*** is **S19**. More information on this subject will be addressed in the section of ECP model. Both the values of $\Delta\nu_{st}$ and the intensity ratio of 0−1 versus 0−0 band (I_{01}/I_{00}) decrease in the order **S7** > **S10** > **S13** > **S16** > **S19mb** > **S19** > **S22**. This is consistent with the expected scenario of a smaller extent of structural relaxation and vibrational coupling in the fluorescing state for larger π systems.[15,27] However, unlike most one-dimensional rigid π systems such as **R*n***, the absorption and fluorescence spectra have poor mirror images due to the presence of more absorption bands. For example, the absorption spectrum of **S7** displays an intense band at 356 nm in addition to the 0−0 (412 nm) and 0−1 (390 nm) bands. Evidently, the presence of an ortho branch is essential for observing these additional optically allowed short-wavelength bands. The ortho segment in **S7**, **S10**, **S13**, and **S22** contains 3, 4, 5, and 8 para-linked phenylene rings, corresponding to **R3**, **R4**, **R5**, and **R8**, respectively. The observed short-wavelength bands of the former group are at longer wavelengths than the 0−0 absorption bands of latter group (i.e., 356, 386, 402, and 442 vs 347, 375, 396, and 433 nm, Table 1). Thus, the short-wavelength bands for **S*n*** should not be due to a localized transition of the ortho-branched arm. On the basis of the TD-DFT calculations (vide infra), these bands involve molecular orbitals localized in the two meta-related arms.

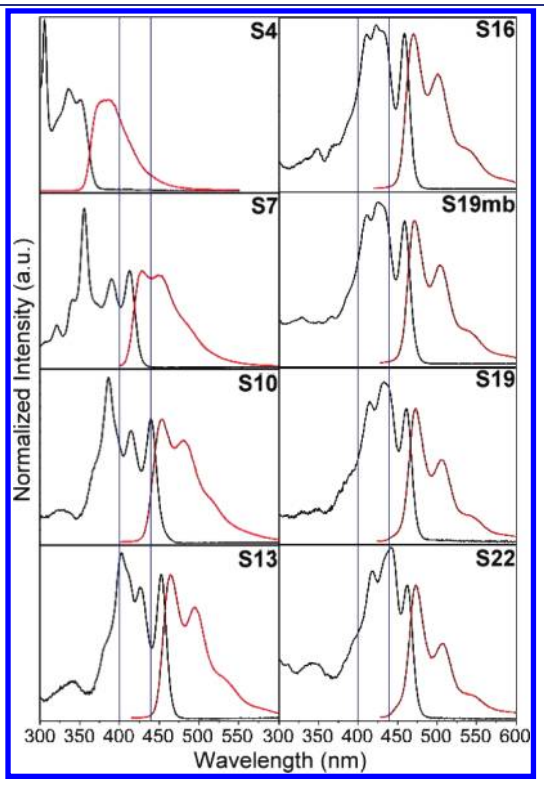

Figure 2. Normalized absorption (black) and fluorescence (red) spectra for **S*n*** in CH_2Cl_2 at room temperature. The two vertical blue lines denote the positions of 400 and 440 nm for the discussion of the results of time-resolved fluorescence anisotropy.

The fluorescence quantum efficiencies (Φ_{fl})[28] and fluorescence lifetime (τ_{fl}) for **S*n*** in CH_2Cl_2 are also shown in Table 1. Except for **S4** that displays a lower value of Φ_{fl} (0.63), the other **S*n*** have similar fluorescence quantum yields (Φ_{fl} = 0.80−0.84). In contrast, the values of τ_{fl} show a progressive decrease from **S4** to **S22**, although **S19mb** has the same lifetime as **S16**. Thus, the radiative decay rate constant k_{fl} ($k_{fl} = \Phi_{fl}/\tau_{fl}$) increases as the *n* increases. The smaller k_{fl} for **S19mb** vs **S19** highlights the negative effect of skeletal branching on k_{fl}. Skeletal branching might also account for the smaller k_{fl} for **S*n*** vs **R*n*** of the same number of phenylene rings (e.g., **S4** vs **R4**).

The electrochemical behavior of **S*n*** has been investigated by cyclic voltammetry (CV) and differential pulse voltammetry (DPV). As shown in Figure 3, the number of reversible anodic waves increases from one for **S4** to four for **S13**. Several reversible anodic waves are also present for the larger **S*n***, but the peaks become less resolved. Nevertheless, it can be concluded that the larger is the **S*n*** size, the more charges can be accommodated. The oxidation potentials (E_{ox}) relative to the ferrocene redox couples based on the DPVs are shown in Table 1. As the *n* value increases, both the first and the second oxidation potentials (E_{ox1} and E_{ox2}) of **S*n*** undergo negative shifts (i.e., **S4** > **S7** > **S10** > **S13** > **S16** > **S19** = **S19mb** > **S22**). The same trend also hold for the size of peak splitting between E_{ox1} and E_{ox2}

Table 1. Photophysical and Electrochemical Data for S*n* and R*n* in CH_2Cl_2 at Room Temperature

compd	λ_{abs}[a] (nm)	log ε[b]	λ_{fl}[c] (nm)	$\Delta\nu_{st}$[d] (cm^{-1})	Φ_{fl}	τ_{fl} (ns)	k_{fl}[e] (10^8 s^{-1})	E_{ox}[f] (V)
S4	306 336 (352)	4.46 (4.19)	(382)[g]	2231	0.63	3.22	1.96	(0.79)
S7	356 390 (412)	5.03 (4.81)	(428) 449	907	0.81	1.97	4.11	(0.57) 1.05
S10	386 415 (439)	5.16 (5.03)	(453) 481	704	0.84	1.38	6.09	(0.48) 0.85 1.14
S13	402 426 (452)	5.27 (5.21)	(464) 495	572	0.83	1.16	7.16	(0.44) 0.75 0.92 1.15
S16	411 430 (458)	5.31 (5.27)	(470) 500	557	0.80	1.03	7.77	(0.43) 0.70 0.80 0.96
S19mb	411 425 (459)	5.31 (5.26)	(471) 503	555	0.81	1.03	7.86	(0.41) 0.66 0.84
S19	414 433 (461)	5.41 (5.33)	(472) 506	506	0.81	0.91	8.90	(0.41) 0.66 0.80
S22	418 442 (462)	5.52 (5.41)	(472) 507	458	0.82	0.83	9.88	(0.38) 0.59 0.89
R2	(305)	(3.85)	(312)	736	0.28	4.04	0.69	
R3	314 (347)	(4.63)	(353) 366	490	0.38	2.01	1.89	1.02
R4	357 (375)	(4.88)	(382) 401	489	0.78	1.36	5.74	0.83
R5	375 (396)	(5.04)	(403) 425	439	0.81	1.12	7.23	0.75
R8[h]	410 (433)		(441) 469					

[a] Peak maxima of the absorption bands with the 0−0 band in the parentheses. [b] Extinction coefficients of the highest peak and the 0−0 absorption band with the latter in parentheses. [c] Maxima of the 0−0 and 0−1 fluorescence bands with the former in parentheses. [d] Stokes shift defined by the difference of the 0−0 absorption and fluorescence peak maxima. [e] $k_{fl} = \Phi_{fl}/\tau_{fl}$. [f] Oxidation potentials vs Fc/Fc^+ with the first oxidation potential (E_{ox1}) in parentheses. [g] Estimated from the blue edge of the fluorescence plateau. [h] Data from ref 7.

dx.doi.org/10.1021/ja202144v |*J. Am. Chem. Soc.* 2011, 133, 8028–8039

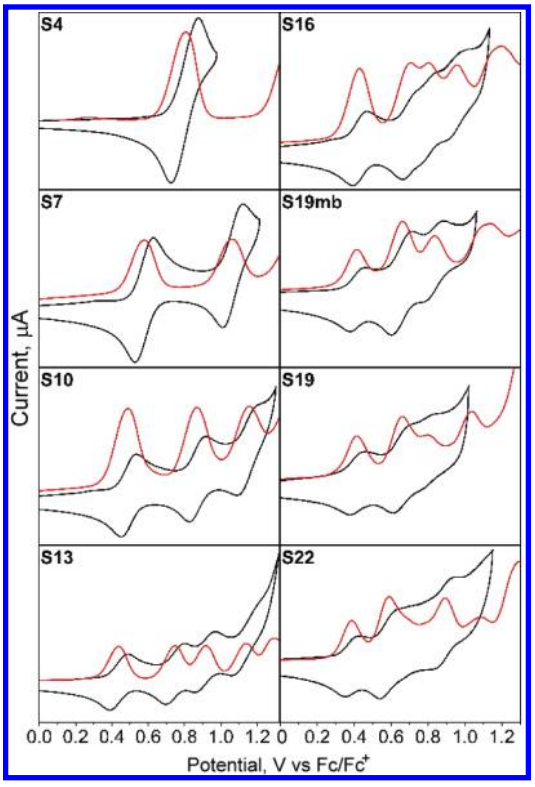

Figure 3. Cyclic voltammogram (black) and differential pulse voltammogram (red) for oxidation of **S*n*** in CH_2Cl_2 with electrolyte 0.1 M Bu_4NPF_6 at a scan rate of 100 mV s^{-1}.

($\Delta E_{ox} = E_{ox2} - E_{ox1}$). The smaller ΔE_{ox} for larger **S*n*** can be attributed to a decreasing Coulombic repulsion between the two charges. The behavior of *n*-dependent charge accommodation and peak splitting has also been observed for the stepladder analogues of **S*n*** (i.e., **SF*n***).[15] However, the E_{ox1} of **SF*n*** (0.60 V vs Fc/Fc^+) is independent of the *n* values (10, 16, and 22) and lies in between that of **S4** (0.79 V) and **S7** (0.57 V), the result of which reflects the important effect of structural planarity (or conformational freedom in torsions) on electronic properties.

ECP Model. MCO are ideal models for elucidating fundamental electronic properties of π-conjugated polymers. Correlation plots of photophysical or electrochemical data against the number of repeat units (n) or its reciprocal (1/n) are particularly informative.[17,18,29] For example, the ECL and the limiting bandgap of many one-dimensional systems have been determined on the basis of the optical transition energy vs 1/n plots.[17] In addition, the interplay of charge transfer and conjugation (particle in a box) interactions in donor−acceptor substituted MCO can be probed with the spectral peak maxima vs n plots.[29] With the correlations known for the parent systems, any deviation of related compounds might reveal the conformational or substituent effects. As such, data of the electronic 0−0 energy and the first oxidation potential of **R*n*** and **S*n*** in CH_2Cl_2 are plotted against 1/n, where n is the number of phenylene rings for consideration. To study the temperature and solvent effects on the 0−0 energies and thus the correlation plots, we have also determined the fluorescence and excitation spectra of **R*n*** and **S*n*** in methylcyclohexane (MCH) at 77 and 300 K (Figure S1, SI). The corresponding 0−0 band energies are shown in Table S1,SI.

Plots a−f in Figure 4 show the excellent linear correlations ($r^2 > 0.997$) for the 0−0 band energies of absorption,

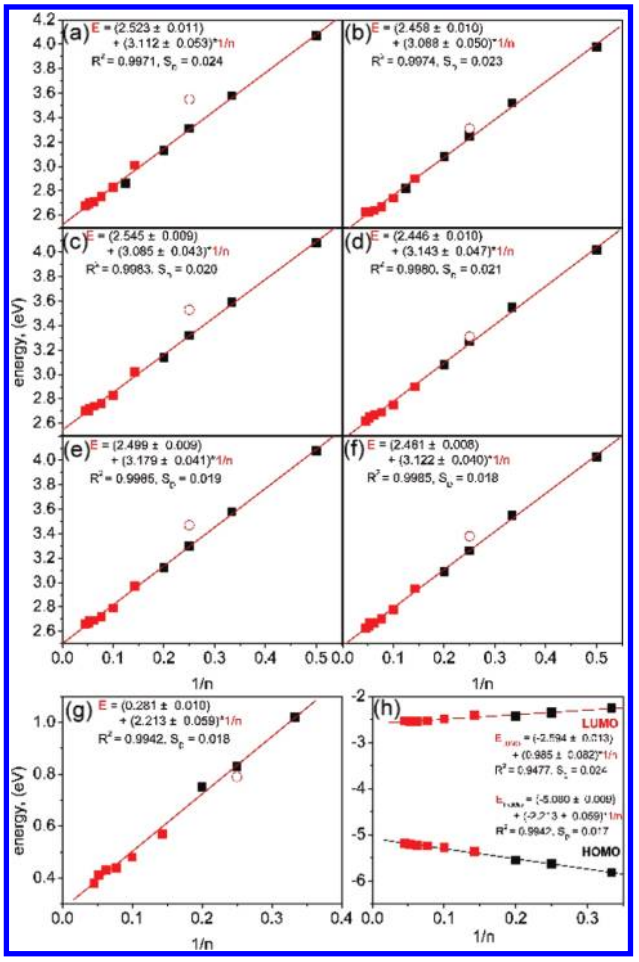

Figure 4. Linear plots of the 0−0 band energy (eV) of the (a) absorption and (b) fluorescence in CH_2Cl_2 at room temperature, the (c) excitation and (d) fluorescence in MCH at 300 K, the (e) excitation and (f) fluorescence in MCH at 77 K, and the plots of (g) the first oxidation potential (E_{ox1}) and (h) HOMO and LUMO energy levels (eV) versus the reciprocal of number of the backbone phenylene rings ($n = n$) in **S*n*** (red squares) and **R*n*** (black squares). The red open circle specifically denotes **S4** for the purpose of discussion.

fluorescence, or excitation spectra against 1/n with n = *n* for both **S*n*** ($n = 7, 10, 13, 16, 19, 22$) and **R*n*** ($n = 2-5$ and/or 8). In contrast, poorer correlations ($r^2 < 0.990$, Figure S2 in SI) were found with considering only the para-conjugated oligophenylene chain of **S*n*** (i.e., $n = (2n + 1)/3 = 5, 7, 9, 11, 13, 15$ for **S7**, **S10**, **S13**, **S16**, **S19**, and **S22**, respectively, and n = 11 for **S19mb**). This explicitly shows that electronic excitation is effectively delocalized over the whole two-dimensional π-backbone of **S*n*** in both the ground and the fluorescing state configurations. In other words, the ortho conjugation is as effective as the para conjugation in **S*n*** in lowering the energy gap, and each **S*n*** molecule behaves as a single chromophore. Fully two-dimensional exciton delocalization has not been observed for other branched MCO,[30,31] including the stepladder systems **SF*n***.[15] Oligophenylenes **SF16** and **SF22** display the same fluorescence 0−0 energy at 438 nm (2.83 eV), which is red-shifted by only 8 nm from the 0−0 band of **SF10** (430 nm, 2.88 eV).[15] We might conclude that it requires ortho−para connectivity and torsion-constrained planar π-scaffolds to achieve two-dimensional exciton delocalization.[32] In fact, only few known two-dimensional systems can fulfill both criteria.

dx.doi.org/10.1021/ja202144v |*J. Am. Chem. Soc.* 2011, 133, 8028–8039

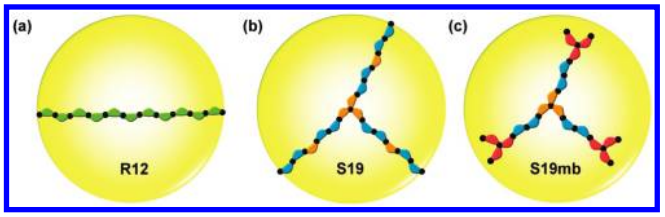

Figure 5. Model proposed for the effective conjugation plane (ECP, a two-dimensional region covered by the yellow circle) of conjugated systems illustrated with (a) **R12**, (b) **S19**, and (c) **S19mb**.

Disc-shaped polycyclic aromatic hydrocarbons (PAHs)[33−35] such as coronene and hexa-*peri*-hexabenzocoronene (HBC) are also qualified for two-dimensional exciton delocalization. Two-dimensional PAHs with a continued small curvature would lead to three-dimensional bowl- (e.g., corannulene)[36] or ball-shaped (e.g., C_{60})[37] structures. Their low HOMO−LUMO gaps appear to demonstrate an effective two- or three-dimensional exciton delocalization. Nevertheless, these PAHs are not oligomers of well-defined repeat unit and thus cannot be analyzed like **S*n*** with the correlation plots.

The observation of two-dimensional conjugation in the excited state of **S*n*** has led us to propose the ECP model for the description of exciton coherence size (Figure 5). By an analogy to ECL that defines the maximum length of exciton delocalization on one-dimensional systems, the ECP is the maximum region of exciton delocalization in a two-dimensional system. The ECL for **R*n*** has been shown to be approximately the size of **R12** on the basis of single-molecule spectroscopic analysis of **R11** and long-chain **R*n*** ($n \approx 62$ and 165).[22] According to Figure 4 and Table 1, **S19** is approaching the ECP for **S*n***, as both **S19** and **S22** have the same λ_{fl} of 472 nm. The slightly bended para chain in **S19** contains 13 phenylene rings, which has a similar end-to-end distance to the ECL for **R*n*** (i.e., the diameter of the yellow circle in Figure 5). This appears to suggest that ECP and ECL have a common origin: namely, exciton delocalization is multidimensional in nature with a specific size (e.g., a 3D sphere or 2D circle), but only suitable multidimensional systems can manifest this nature. To the best of our knowledge, **S*n*** is the first system that uncovers the two-dimensional boundary of exciton delocalization. Nevertheless, our results indicate that the ECL of one-dimensional systems allows one to define the diameter.

In the context of the ECP model, we can address the implications of deviation of **S4** from the linear plots in Figure 4a−f. Regarding the structureless fluorescence for **S4** at room temperature, the fluorescence 0−0 energy was estimated by the blue edge of the fluorescence plateau. The same degree of deviation for **S4** in CH_2Cl_2 at room temperature vs MCH at 300 K (plots a and b vs c and d in Figures 4, respectively) indicates a negligible solvent polarity effect. However, at 77 K the deviation becomes smaller and larger in the excitation (Figure 4e) and the fluorescence energy plot (Figure 4f), respectively. All these observations can be attributed to a conformation effect. According to the X-ray crystal structures of **R5**,[6] **S4**,[16] and **S7**,[16] the arms of **S*n*** are planar but the isotruxene core has a small twist (9.8° for **S4** and 18.6° for **S7**) between the two ortho-branched phenylene rings due to steric hindrance. This backbone twisting in the ground state can account for the blue shift of absorption and excitation spectra for **S4** vs **R4**, although it is not large enough to inhibit exciton delocalization. However, the backbone twisting is expected to be reduced in the excited state due to structural relaxation (planarization), which accounts for the decreased deviation in the fluorescence plots. The occurrence of structural relaxation is also consistent with the structureless fluorescence spectra and the large Stokes shift for **S4** at room temperature. When the compounds are in the MCH glass at 77 K, structural relaxation toward the planar geometry in S_1 is somewhat hampered. This accounts for the increased deviation in the fluorescence energy plot. Since structural relaxation is reduced at 77 K, the more planar conformers in the ground state would contribute more to the excitation spectra. This would lead to a red-shifted excitation spectrum as compared to that recorded at 300 K and thus a smaller deviation for **S4** in Figure 4e. Although the isotruxene cores in **S7** and the larger **S*n*** systems are also nonplanar, the steric effect appears to be negligible. This can be attributed to a dilution of wave functions in the isotruxene core in **S*n*** larger than **S4**. Note that the pattern of ring-bridging substituents in **S4** vs **R4** is more different than that in **1s** vs **1a**. The phenomenon of same fluorescence 0−0 energy but different absorption 0−0 energy for **S4** and **R4** (Table 1) suggests that backbone planarity is more important than substituent pattern in determining the electronic properties.

The above discussion also leads to the conclusion that the small blue shifts of the 0−0 absorption and fluorescence band (3−4 nm) for **S19mb** vs **S19** mainly result from a less planar backbone. The participation of the three terminal ortho-branched phenylene rings in **S19mb** in the conjugation interactions is evidenced by the red-shifted 0−0 absorption and fluorescence bands and lower E_{ox1} value as compared to **S16** (Table 1). However, the presence of four isotruxene groups in **S19mb** makes the density of ortho branching (number of ortho branches/number of phenylene rings = 0.21) to an extent similar to that in **S4** (0.25). Accordingly, the steric effect cannot be neglected in **S19mb**.

A linear correlation between E_{ox1} and 1/n is also observed for **S*n*** and **R*n*** (Figure 4g). Figure 4h shows the corresponding plots with the HOMO and LUMO energy levels that are derived according to eqs 1 and 2:[38]

$$E_{HOMO} = -(4.8 + E_{ox1}) \quad (1)$$

$$E_{LUMO} = E_{HOMO} + E_{0,0} \quad (2)$$

where $E_{0,0}$ is the 0−0 transition energy obtained from the intersection of normalized absorption and fluorescence 0−0 bands. The results show that increasing the chain length destabilizes the HOMO but stabilizes the LUMO and thus reduces the optical bandgap. A larger slope for the HOMO (−2.23) vs the LUMO (0.99) plot also reveals that the HOMO energy is more sensitive than that of the LUMO to the chain length, as is the case in linear oligophenylenes.[4]

Electronic Structure. We have shown that, unlike the multichromophoric nature of most multidimensional MCO,[31] the **S*n*** represent the first example of single chromophores with branched arms. To gain insight into the electronic structure and spectra of **S*n***, we have carried out DFT calculations for the ground-state geometry optimization and TD-DFT calculations for the absorptions in the B3LYP/6-31G** level.[39,40] To expedite the calculations, all the solubilizers on the saturated carbons are replaced with methyl groups. The energy diagram of the highest occupied molecular orbital HOMO (H) and lowest unoccupied molecular orbital LUMO (L) and the nearby orbitals H−2,

H−1, L+1, and L+2 for **S*n*** are shown in Figure 6. These frontier molecular orbitals (FMO) for **S19** are shown in Figure 7, and the corresponding FMO for the other **S*n*** are shown in SI: Figure S3. The calculated absorption wavelength ($\lambda_{abs,cal}$), oscillator strength (f), and the configuration description of the lowest three singlet excited states (S_1-S_3) are shown in Table 2. For comparison, the corresponding calculations for **R2**−**R5** were also carried out, and the results are shown in SI: Table S2 and Figure S3.

Despite a large difference in the number of phenylene rings (n = 4−22) and ortho-branching (4 in **S19mb** but 1 in the others) in **S*n***, they have a great similarity in the calculated electronic structure. There are two allowed transitions for each **S*n***, which are $S_0 \rightarrow S_1$ and $S_0 \rightarrow S_3$ for **S4**, **S7**, and **S10** but the latter transition becomes $S_0 \rightarrow S_2$ for the larger **S*n***. Disregarding the second allowed transition being $S_0 \rightarrow S_2$ or $S_0 \rightarrow S_3$, it possesses a larger f value than the $S_0 \rightarrow S_1$ transition for all cases. This is consistent with the absorption spectra, where the maximum is always located at shorter wavelengths than the 0−0 absorption bands for **S*n*** (Figure 2). For all **S*n***, the S_1 state is mainly

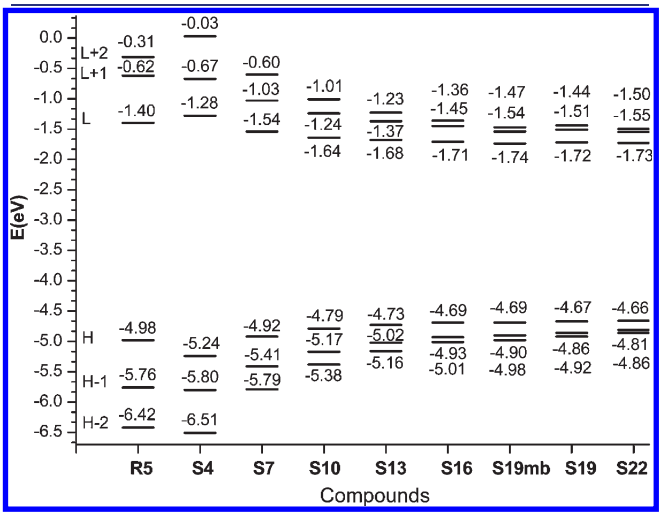

Figure 6. B3LYP/6-31G** orbital energy level diagram for **S*n*** and **R5**.

contributed by the H → L configuration and the allowed S_2 or S_3 excitation is dominated by two configurations, H−1 → L and H → L+1, although there are more configuration interactions as the size of **S*n*** increases. The increased participation of the configurations associated with the H−2 and L+2 orbitals in the allowed transitions for larger **S*n*** could be attributed to the significantly decreased energy difference between orbitals H−2 and H−1 and orbitals L+1 and L+2 (Figure 6). As represented by the case of **S19** (Figure 7), the H, L, H−2 and L+2 cover all the phenylene backbone with larger electron density in the central vs terminal phenylene rings for the former two orbitals but an opposite electron distribution is observed for the latter two orbitals. In contrast, the molecular orbitals H−1 and L+1 have electron density localized on the two arms that are meta-related with respect to the central phenylene ring. Evidently, the $S_0 \rightarrow S_1$ is a completely delocalized transition, in agreement with the conclusion based on the $1/n$-correlated 0−0 energy plots (Figure 4). Although the second allowed $S_0 \rightarrow S_2$ transition is somewhat localized in the two meta-related arms, the two major configurations involve both the delocalized molecular orbitals H and L and have opposite direction of electron motions: from the localized H−1 to the delocalized L and from the delocalized H to the localized L+1.

Another interesting feature for the two allowed transitions for **S*n*** is their distinct orientation of the transition dipole moments, which is different from the linear analogues **R*n***. As represented by **S19** again, the orientations of the two allowed transition moments are depicted in Figure 8. The other **S*n*** all display similar orientations for the two allowed transitions (Figure S4 in SI). These two allowed transition dipoles defines an angle (θ) in the range 65−73° for **S*n***. In contrast, there is only one allowed transition $S_0 \rightarrow S_1$ that is oriented along the long molecular axis for **R5**, and the calculated oscillator strengths for the transitions to S_2 and higher singlet states are essentially zero (Table S2). This character is retained for larger **R*n*** but not for the smaller systems. For example, **R2** (9,9-dialkylfluorene) has transitions moments oriented along the short (S_3 and S_5) molecular axis in a comparable size as those along the long (e.g., S_1, S_2, and S_4) molecular axis (Figure S4). Evidently, the electronic structure of **R2** resembles most small molecule chromophores with

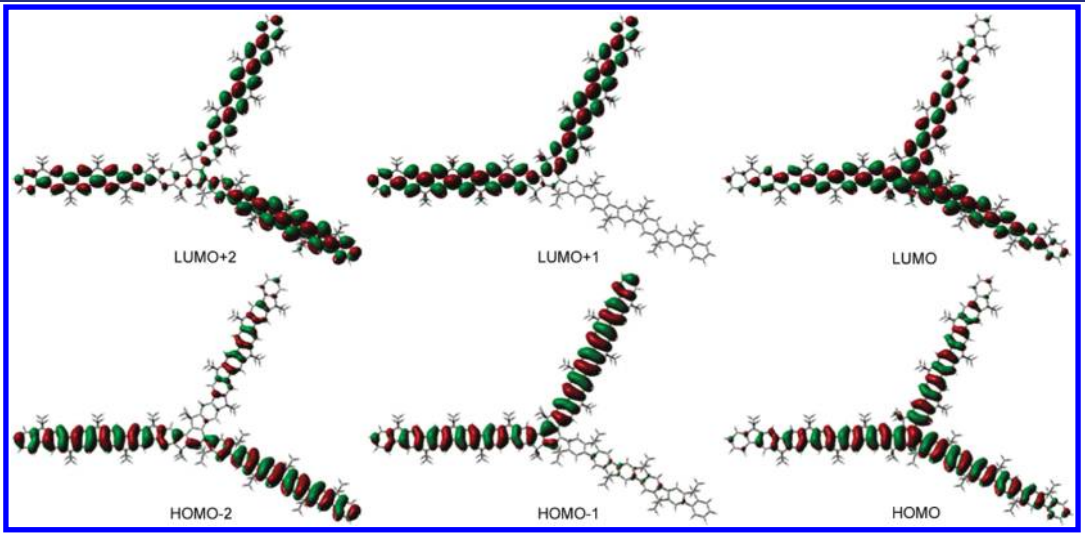

Figure 7. B3LYP/6-31G** level calculated structure and the frontier molecular orbitals of **S19**. Only atomic charge densities with 1% or higher contribution are included.

dx.doi.org/10.1021/ja202144v | J. Am. Chem. Soc. 2011, 133, 8028–8039

Table 2. B3LYP/6-31G Level Calculated Absorption Energy, Oscillator Strength, and Description for the Lowest Three Singlet Excited States of S*n***

compd	excited state	$\lambda_{abs,cal}$[a] (nm)	f[b]	configuration[c]	weight[d] (%)
S4	S_1	343	0.404	H → L	98
	S_2	328	0.004	H−1 → L	49
				H → L+1	48
	S_3	295	0.522	H−1 → L	46
				H → L+1	48
S7	S_1	410	0.888	H → L	99
	S_2	371	0.006	H−1 → L	50
				H → L+1	45
	S_3	355	1.170	H−1 → L	46
				H → L+1	52
S10	S_1	444	1.425	H → L	98
	S_2	396	0.114	H−1 → L	68
				H → L+1	26
	S_3	393	1.710	H−1 → L	27
				H → L+1	69
S13	S_1	462	1.949	H → L	96
	S_2	418	2.420	H−1 → L	59
				H → L+1	35
	S_3	410	0.030	H−1 → L	35
				H → L+1	58
S16	S_1	473	2.497	H → L	94
	S_2	434	3.059	H−1 → L	52
				H → L+1	37
	S_3	420	0.013	H−1 → L	40
				H → L+1	52
S19mb	S_1	481	2.522	H → L	92
	S_2	446	2.873	H−1 → L	41
				H−1 → L+2	5
				H → L+1	44
	S_3	427	0.007	H−1 → L	49
				H → L+1	43
S19	S_1	479	3.041	H → L	91
	S_2	445	3.691	H−2→ L+1	5
				H−1 → L	47
				H−1 → L+2	5
				H → L+1	36
	S_3	426	0.007	H−1 → L	42
				H → L+1	47
S22	S_1	484	3.605	H → L	88
	S_2	454	4.317	H−2 → L+1	6
				H−1 → L	43
				H−1 → L+2	7
				H → L+1	35
	S_3	431	0.019	H−2 → L	15
				H−1 → L	40
				H → L+1	35

[a] Calculated absorption energy. [b] Oscillator strength. [c] H and L stand for HOMO and LUMO, respectively. The second and third highest occupied molecular orbitals are denoted as H−1 and H−2 and the second and third lowest unoccupied molecular orbitals as L+1 and L+2, respectively. [d] Only configurations with 5% or greater contribution are included.

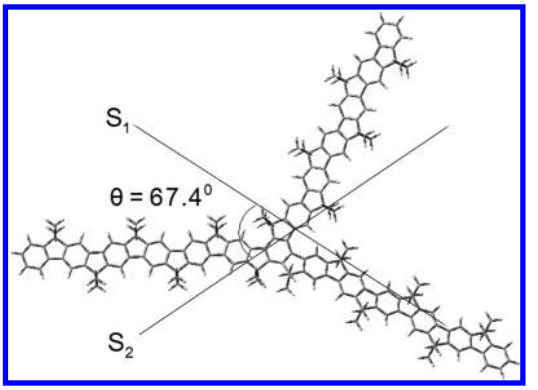

Figure 8. Orientation of the transition dipoles for the B3LYP/6-31G** level calculated $S_0 \rightarrow S_1$ and $S_0 \rightarrow S_2$ absorptions of **S19**.

two-dimensionally spread transition moments, but **R5** behaves as linear π-conjugated polymers, which are characterized by one-dimensional polarization that leads to a single intense structured absorption band. In this context, the behavior of **S*n*** is more molecule-like than polymer-like. The two-dimensional optical transition character for **S*n*** is indeed borne out by their wavelength-dependent fluorescence anisotropy (vide infra).

The calculated absorption wavelength for the S_1 state is in the order **S22** > **S19mb** > **S19** > **S16** > **S13** > **S10** > **S7** > **S4**, which is consistent with the experimental observation except for the position of **S19mb**. The observed 0−0 absorption energy for **S19mb** is 2 nm lower than that of **S19**, but the opposite (2 nm higher) was predicted by the TD-DFT calculations. This discrepancy could be attributed to the uncertainty raised by the level of theoretical approach. If this factor can be ruled out, other possible differences may lie in the backbone planarity. The calculated structures are expected to have more planar phenylene backbone in the isotruxene moieties because of the use of smaller methyl substituents. This in turn suggests that with a more planar phenylene backbone the phenylene connection in **S19mb** would lower the energy gap more than that in **S19**. This might be attributed to the smaller diameter of **S19mb** vs **S19** (Figure 5) in view of the fact that the HOMO and LUMO have more electron density in the center than the terminals (Figure 7). Recall that the $S_0 \rightarrow S_1$ transition is mainly from the HOMO → LUMO configuration. The calculated results also support the conclusion from the energy plots (Figure 4) that ortho conjugation is inherently as effective as para conjugation. The commonly observed weaker electronic coupling through an ortho-phenylene bridge results from a steric effect that decreases the backbone planarity.

Fluorescence Anisotropy. To verify the TD-DFT predicted two-dimensional optical transition character of **S*n***, we have measured the time-resolved fluorescence anisotropy for **S*n*** ($n \geq 7$) in CH_2Cl_2 with two different excitation wavelengths (400 and 440 nm, the blue lines in Figure 2). For comparison, the corresponding measurement was carried out for **R5**. Figure 9 shows the polarized fluorescence decay curves for **S19** and **R5** recorded at angles of 0° (parallel, $I_{\parallel}$), 54.7° (magic angle, I_{MA}), and 90° (perpendicular, $I_{\perp}$) with respect to the polarization direction of the excitation laser. The corresponding decay curves for the other compounds are provided in the Supporting Information (Figure S5). Measured polarized fluorescence decay curves are carefully scaled by the tail-matching method to correct different grafting efficiencies for $I_{\parallel}$ and $I_{\perp}$, in order to calculate

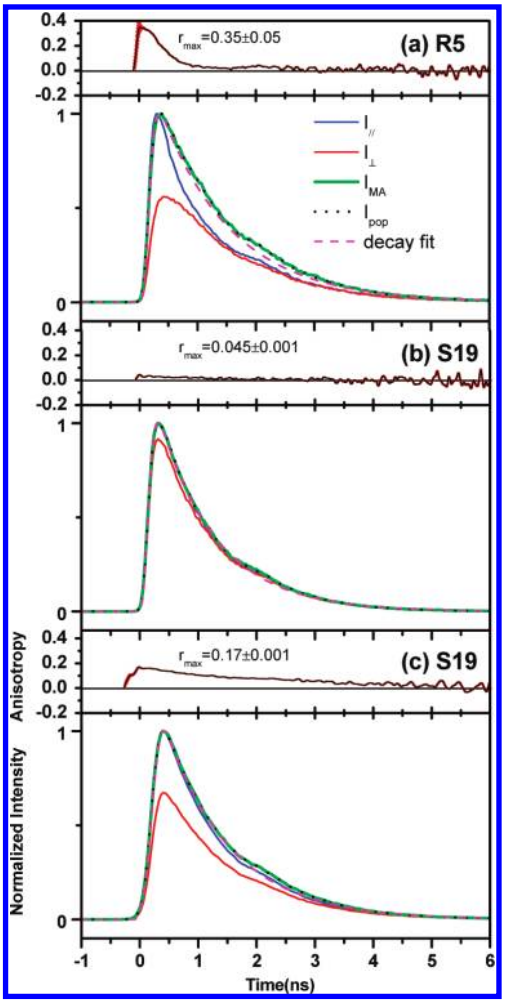

Figure 9. Fluorescence and anisotropy decay curves for (a) **R5** and (b) **S19** excited at 400 nm and for (c) **S19** excited at 440 nm. The solvent is CH_2Cl_2. Solid line denotes the measured polarized fluorescence decay curves in blue ($I_{\parallel}$), red ($I_{\perp}$), and green (I_{MA}). Dotted black line denotes the constructed population decay curve (I_{pop}), while magenta dashed line denotes the fitting curve. Anisotropy decay curve is shown as a solid black line with estimated error in red shadow area.

fluorescence anisotropy r based on eq 3:[41]

$$r = \frac{I_{\parallel} - I_{\perp}}{I_{\parallel} + 2I_{\perp}} = \frac{2}{5}\langle P_2(\cos\theta)\rangle \qquad (3)$$

where $P_2(\cos(\theta))$ is the second Legendre Polynomial ($P_2(x) = 0.5(3x^2 - 1)$) of the cosine of the angle between the absorption and emission dipole moments. A constructed population decay curve, $I_{pop} = 1/3 \cdot (I_{\parallel} + 2I_{\perp})$ of **R5** (Figure 9a), which is physically as meaningful as I_{MA}, is nearly identical to the polarized decay curve monitored at magic angle (I_{MA}) after normalization. This further supports proper setup and alignment for the polarizer and the reliability of our anisotropy measurements. The resulting anisotropy decay curves are also shown in Figure 9, and the calculated time−zero anisotropy (r) values are depicted in Figure 10. Evidently, the anisotropy of **S*n*** depends on both the n value and the excitation wavelength. At 440 nm, the anisotropy r values are all positive and in the order **S10** > **S13** > **S22** > **S16** ≈ **S19mb** ≈ **S19**. The anisotropy decreases for them on going from 440 to 400 nm, and the sign becomes negative for

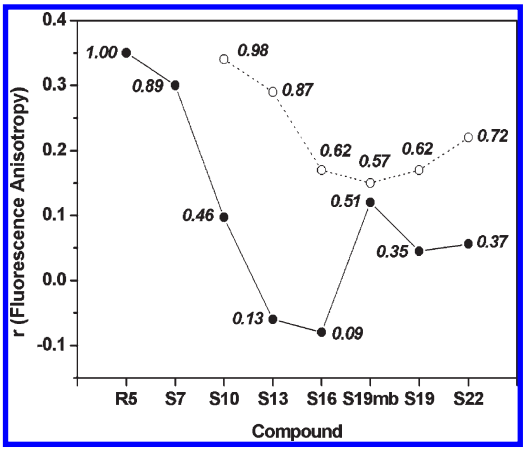

Figure 10. Fluorescence anisotropy for **S*n*** and **R5** in CH_2Cl_2 with the excitation wavelengths at 400 (solid circles and lines) and 440 nm (open circles and dashed lines). The number for each data point denotes the fraction of contribution from the $S_0 \rightarrow S_1$ absorption (f_1(400 nm) for the solid circles and f_1(440 nm) for the open circles) calculated based on eq 5.

S13 and **S16**. At 400 nm, **R5** and **S7** can also be determined, and they display higher anisotropy than the other **S*n***.

The results shown in Figure 10 can be rationalized by the changing contributions of the two allowed transitions ($S_0 \rightarrow S_1$ and $S_0 \rightarrow S_2$ or S_3), which have transition moments polarized at an angle (θ) of 65−73° to each other based on TD-DFT calculations (vide supra). The validity of a large calculated θ angle between the two allowed transitions is promptly supported by the negative r values observed for **S13** and **S16**, since θ values smaller than the magic angle 54.7° will lead to only positive r values. Assuming that the emission dipole moment is collinear to the $S_0 \rightarrow S_1$ transition dipole (i.e., $\theta = 0$), the $S_0 \rightarrow S_1$ and $S_0 \rightarrow S_2$ transitions would lead to theoretical r values of 0.4 and −0.11 to −0.15, respectively, according to eq 3. In general, the observed limiting anisotropy is less than the theoretical value 0.4. The high r value of 0.35 observed for **R5** excited at 400 nm is likely approaching the limiting anisotropy in this work. Note that the excitation corresponds to the 0−0 $S_0 \rightarrow S_1$ transition (Figure S1 in SI) and transitions to higher singlet excited states are predicted to be forbidden for **R5** (Table S2 in SI). The r value for **S10** excited at 440 nm is also high (0.34), consistent with a nearly pure $S_0 \rightarrow S_1$ transition by inspecting its absorption spectrum (Figure 2). Assuming that the other minor transitions are negligible at the excitation wavelengths, the relative fraction of contributions of the two allowed transitions (f_1 and f_2) can be estimated by the determined r values at any excitation wavelength λ based on eqs 4−6.

$$r(\lambda) = f_1(\lambda)r_1 + f_2(\lambda)r_2 \qquad (4)$$

$$f_1(\lambda) = (r(\lambda) + 0.12)/0.47 \qquad (5)$$

$$f_2(\lambda) = (0.35 - r(\lambda))/0.47 = 1 - f_1(\lambda) \qquad (6)$$

where r_1 and r_2 are the limiting anisotropy of the $S_0 \rightarrow S_1$ and $S_0 \rightarrow S_2$ or S_3 transitions. With the assumption of $r_1 = 0.35$ based on the data for **R5** and **S10**, the value of r_2 is predicted to be −0.12 for $\theta = 69°$ (i.e., the average θ value for the second allowed transition with respect to the $S_0 \rightarrow S_1$ transition in **S*n***). The calculated f_1 values for **S*n*** are shown in Figure 10, and they agree

dx.doi.org/10.1021/ja202144v |J. Am. Chem. Soc. 2011, 133, 8028–8039

reasonably well with the appearance of absorption spectra shown in Figure 2 (marked with blue lines). More detailed data for θ, r, f_1, and f_2 are shown in Table S3 (Supporting Information).

CONCLUSION

Our systematic studies on the ortho-branched ladder-type MCO **S*n*** show that each **S*n*** is a molecule-like single chromophore covering all the n phenylene rings in the backbone, including the multibranched case (**S19mb**). This in turn leads to the following implications. First, exciton delocalization through an ortho-phenylene bridge is as efficient as that through a para-phenylene bridge provided that the π-conjugated backbone is free from large torsion angles and torsional motions. In this context, isotruxene is a useful building block for constructing ortho-branched systems of effective two-dimensional conjugation. Second, backbone planarity plays the most important role in determining the size of electron coupling among the oligomeric π-segments than the substituted patterns of solubilizers. Third, exciton delocalization is multidimensional (or nondirectional) in nature, and the effective conjugation plane for a two-dimensional system possesses a diameter equivalent to the effective conjugation length defined by linear MCO analogues. This information should be valuable for developing novel multidimensional π-conjugated systems of desired electronic properties such as low bandgap, large two-photon absorption cross section,[42] and high charge-carrier mobility.[43]

EXPERIMENTAL SECTION

Materials. All commercially available materials were used as received. Solvents for photochemical and electrochemical measurements were HPLC grade. CH_2Cl_2 was dried by calcium hydride and distilled before use. Detailed synthetic procedures and structural characterization data for new compounds are provided as Supporting Information.

Methods. All the spectral and electrochemical data were collected at room temperature (23 ± 1 °C). UV−visible spectra were measured on a Cary300 double beam spectrophotometer. Fluorescence spectra were recorded on a PTI QuantaMaster C-60 spectrometer and corrected for instrumental nonlinearity. The optical density (OD) of all solutions was about 0.1 at the wavelength of excitation. Fluorescence quantum yields were determined using an integrating sphere (150 mm diameter, $BaSO_4$ coating) of Edinburgh Instruments by the Edinburgh FLS920 spectrometer. Fluorescence decays were also measured at room temperature with the use of the Edinburgh FLS920 spectrometer with a gated hydrogen arc lamp using a scatter solution to profile the instrument response function. The goodness of the nonlinear least-squares fit was judged by the reduced χ^2 value (<1.2 in all cases), the randomness of the residuals, and the autocorrelation function. The excitation and fluorescence spectra at 77 K were measured with sample solutions in an Oxford OptistatDN cryostat with an ITC502 temperature controller. Frequency-doubled femtosecond pulses of 400 and 440 nm generated from the Tsunami (Spectra-Physics, U.S.A.) along with an Edinburgh OB900-L spectrometer were used to carry out the time-resolved fluorescence anisotropy measurements. A polarizer was settled in front of the detector and could be tuned to select fluorescence of designated polarization. The cyclic voltammetry (CV) and differential pulse voltammetry (DPV) were recorded on a CHI 612B electrochemical analyzer, and the electrochemical cells adopted a glassy carbon as the working electrode, a Pt wire as a counter electrode, an Ag wire as a reference electrode, and 0.1 M Bu_4NPF_6 as electrolyte. The substrates are ~1 mM in CH_2Cl_2. All reported potentials were calibrated using ferrocene as an internal standard. DFT and TD-DFT calculations were performed with the Gaussian 09 program.[38,39] The gas-phase conformations of **S*n*** and **R*n*** were derived from DFT calculations with B3LYP level of theory and 6-31G** basis set. The electronic nature of the absorption bands was investigated by TD-DFT calculations at the B3LYP/6-31G** level.

ASSOCIATED CONTENT

Supporting Information. Detailed synthetic procedures and characterization data for new compounds, electronic spectra in methylcyclohexane at 77 and 300 K, alternative correlation plots, DFT-calculated molecular orbitals, Cartesian coordinates, orientations of allowed transition dipoles, and full fluorescence anisotropy spectra and data for **S*n*** and **R*n***, TD-DFT-calculated absorption descriptions for **R*n***, and complete ref 39. This material is available free of charge via the Internet at http://pubs.acs.org.

AUTHOR INFORMATION

Corresponding Author
jsyang@ntu.edu.tw; chop@ntu.edu.tw

ACKNOWLEDGMENT

We thank the National Science Council of Taiwan for financial support. We appreciate Prof. Yuan-Chung Cheng of NTU for sharing his computers and software and Prof. Chung-Hsuan Chen, Zhen-Yu Xie, Ting-An Liu, and Hung-Ta Chu for the support on compound characterization. The computing time granted by the Computing Center of NTU is also acknowledged.

REFERENCES

(1) (a) Murphy, A. R.; Fréchet, J. M. J. *Chem. Rev.* **2007**, *107*, 1066–1096. (b) Kim, F. S.; Ren, G.; Jenekhe, S. A. *Chem. Mater.* **2011**, *23*, 682–732.
(2) Gholami, M.; Tykwinski, R. R. *Chem. Rev.* **2006**, *106*, 4997–5027.
(3) Yang, J.-S.; Yan, J.-L.; Lin, C.-K.; Chen, C.-Y.; Xie, Z.-Y.; Chen., C.-H. *Angew. Chem., Int. Ed.* **2009**, *48*, 9936–9939.
(4) Banerjee, M.; Shukla, R.; Rathoore, R. *J. Am. Chem. Soc.* **2009**, *131*, 1780–1786.
(5) (a) Jo, J.; Chi, C.; Höger, S.; Wegner, G.; Yoon, D. Y. *Chem.—Eur. J.* **2004**, *10*, 2681–2688. (b) Feng, X. J.; Wu, P. L.; Tam, H. L.; Li, K. F.; Wong, M. S.; Cheah, K. W. *Chem.—Eur. J.* **2009**, *15*, 11681–11691. (c) He, J.; Crase, J. L.; Wadumethrige, S. H.; Thakur, K.; Dai, L.; Zou, S.; Rathore, R.; Hartley, C. S. *J. Am. Chem. Soc.* **2010**, *132*, 13848–13857.
(6) Wong, K.-T.; Chi, L.-C.; Huang, S.-C.; Liao, Y.-L.; Liu, Y.-H.; Wang, Y. *Org. Lett.* **2006**, *8*, 5029–5032.
(7) Wu, Y.; Zhang, J.; Bo, Z. *Org. Lett.* **2007**, *9*, 4435–4438.
(8) (a) Opsitnick, E.; Lee, D. *Chem.—Eur. J.* **2007**, *13*, 7040–7049. (b) Detert, H.; Lehmann, M.; Meier, H. *Materials* **2010**, *3*, 3218–3330.
(9) (a) Roncali, J.; Leriche, P.; Cravino, A. *Adv. Mater.* **2007**, *19*, 2045–2060. (b) Kanibolotsky, A. L.; Perepichka, I. F.; Skabara, P. J. *Chem. Soc. Rev.* **2010**, *39*, 2695–2728. (c) Tang, W.; Hai, J.; Dai, Y.; Huang, Z.; Lu, B.; Yuan, F.; Tang, J.; Zhang, F. *Sol. Energy Mater. Sol. Cells* **2010**, *94*, 1963–1979. (d) Li, C.; Liu, M.; Pschirer, N. G.; Baumgarten, M.; Müllen, K. *Chem. Rev.* **2010**, *110*, 6817–6855.
(10) Lo, S.-C.; Burn, P. L. *Chem. Rev.* **2007**, *107*, 1097–1116.
(11) (a) Yang, Z.; Xu, B.; He, J.; Xue, L.; Guo, Q.; Xia, H.; Tian, W. *Org. Electron.* **2009**, *10*, 954–959. (b) Jia, H.-P.; Liu, S.-X.; Sanguinet, L.; Levillain, E.; Decurtins, S. *J. Org. Chem.* **2009**, *74*, 5727–5729. (c) Wang, J.-L.; Chan, Y.-T.; Moorefield, C. N.; Pei, J.; Modarelli, D. A.; Romano, N. C.; Newkome, G. R. *Macromol. Rapid Commun.* **2010**, *31*, 850–855. (d) Tang, Z.-M.; Lei, T.; Wang, J.-L.; Ma, Y.; Pei, J. *J. Org. Chem.* **2010**, *75*, 3644–3655. (e) Cui, W.; Fu, Y.; Qu, Y.; Tian, H.; Zhang, J.; Xie, Z.; Geng, Y.; Wang, F. *Chem. Asian J.* **2010**, *5*, 932–940. (f) Ren, S.; Zeng, D.;

Zhong, H.; Wang, Y.; Qian, S.; Fang, Q. *J. Phys. Chem. B* **2010**, *114*, 10374–10383. (g) Zhou, H.; Zhao, X.; Huang, T.; Lu, R.; Zhang, H.; Qi, X.; Xue, P.; Liu, X.; Zhang, X. *Org. Biomol. Chem.* **2011**, *9*, 1600–1607. (h) Zhou, N.; Wang, L.; Thompson, D. W.; Zhao, Y. *Tetrahedron* **2011**, *7*, 125–143. (i) Cornelis, D.; Franz, E.; Asselberghs, I.; Clays, K.; Verbiest, T.; Koeckelberghs, G. *J. Am. Chem. Soc.* **2011**, *133*, 1317–1327.

(12) (a) Ponomarenko, S. A.; Kirchmeyer, S.; Elschner, A.; Huisman, B.-H.; Karbach, A.; Drechsler, D. *Adv. Funct. Mater.* **2003**, *13*, 591–596. (b) Lim, Y.-K.; Jiang, X.; Bollinger, J. C.; Lee, D. *J. Mater. Chem.* **2007**, *17*, 1969–1980. (c) Taerum, T.; Lukoyanova, O.; Wylie, R. G.; Perepichka, D. F. *Org. Lett.* **2009**, *11*, 3230–3233.

(13) (a) Cao, X.-Y.; Zhang, W.-B.; Wang, J.-L.; Zhou, X.-H.; Lu, H.; Pei, J. *J. Am. Chem. Soc.* **2003**, *125*, 12430–12431. (b) Kanibolotsky, A. L.; Berridge, R.; Skabara, P. J.; Perepichka, I. F.; Bradley, D. D. C.; Koeberg, M. *J. Am. Chem. Soc.* **2004**, *126*, 13695–13702. (c) Zhang, W.; Cao, X.-Y.; Zi, H.; Pei, J. *Org. Lett.* **2005**, *7*, 959–962. (d) Han, Y.; Fei, Z.; Sun, M.; Bo, Z.; Liang, W.-Z. *Macromol. Rapid Commun.* **2007**, *28*, 1017–1023. (e) Jiang, Y.; Lu, Y.-X.; Cui, Y.-X.; Zhou, Q.-F.; Ma, Y.; Pei, J. *Org. Lett.* **2007**, *9*, 4539–4542. (f) Oliva, M. M.; Casado, J.; Navarrete, J. T. L.; Berridge, R.; Skabara, P. J.; Kanibolotsky, A. L.; Perepichka, I. F. *J. Phys. Chem. B* **2007**, *111*, 4026–4035.

(14) (a) Melinger, J. S.; Pan, Y.; Kleiman, V. D.; Peng, Z.; Davis, B. L.; McMorrow, D.; Lu, M. *J. Am. Chem. Soc.* **2002**, *124*, 12002–12012. (b) Wang, J.-L.; Yan, J.; Tang, Z.-M.; Xia, Q.; Ma, Y.; Pei, J. *J. Am. Chem. Soc.* **2008**, *130*, 9952–9962.

(15) (a) Yang, J.-S.; Lee, Y.-R.; Yan, J.-L.; Lu, M.-C. *Org. Lett.* **2006**, *8*, 5813–5816. (b) Yang, J.-S.; Huang, H.-H.; Ho, J.-H. *J. Phys. Chem. B* **2008**, *112*, 8871–8878.

(16) Yang, J.-S.; Huang, H.-H.; Liu, Y.-H.; Peng, S.-M. *Org. Lett.* **2009**, *11*, 4942–4945.

(17) Gierschner, J.; Cornil, J.; Egelhaaf, H.-J. *Adv. Mater.* **2007**, *19*, 173–191.

(18) Meier, H.; Stalmach, U.; Kolshorn, H. *Acta Polym.* **1997**, *48*, 379–384.

(19) Van Averbeke, B.; Beljonne, D. *J. Phys. Chem. A* **2009**, *113*, 2677–2682.

(20) (a) Grimsdale, A. C.; Müllen, K. *Adv. Polym. Sci.* **2006**, *199*, 1–82. (b) Grimsdale, A. C.; Müllen, K. *Adv. Polym. Sci.* **2008**, *212*, 1–48.

(21) Wu, Y.; Zhang, J.; Fei, Z.; Bo, Z. *J. Am. Chem. Soc.* **2008**, *130*, 7192–7193.

(22) Schindler, F.; Jacob, J.; Grimsdale, A. C.; Scherf, U.; Müllen, K.; Lupton, J. M.; Feldmann, J. *Angew. Chem., Int. Ed.* **2005**, *44*, 1520–1525.

(23) (a) Wu, Y.; Hao, X.; Wu, J.; Jin, J.; Ba, X. *Macromolecules* **2010**, *43*, 731–738. (b) Sprick, R. S.; Thomas, A.; Scherf, U. *Polym. Chem.* **2010**, *1*, 283–285.

(24) Thirion, D.; Poriel, C.; Rault-Berthelot, J.; Barriére, F.; Jeannin, O. *Chem.—Eur. J.* **2010**, *16*, 13646–13658.

(25) Yang, J.-S.; Huang, H.-H.; Lin, S.-H. *J. Org. Chem.* **2009**, *74*, 3974–3977.

(26) Lin, S.-H.; Hsu, Y.-C.; Lin, J. T.; Lin, C.-K.; Yang, J.-S. *J. Org. Chem.* **2010**, *75*, 7877–7886.

(27) Wasserberg, D.; Dudek, S. P.; Meskers, S. C. J.; Janssen, R. A. J. *Chem. Phys. Lett.* **2005**, *411*, 273–277.

(28) The Φ_f values in Table 1 were determined directly with an integrating sphere. The new data differ from the previously communicated values determined with actinometric methods and are within 10% for all cases except for **S4** (13%).

(29) Meier, H. *Angew. Chem., Int. Ed.* **2005**, *44*, 2482–2506.

(30) (a) Zhou, X.-H.; Yan, J.-C.; Pei, J. *Org. Lett.* **2003**, *5*, 3543–3546. (b) Zhou, X.; Ren, A.-M.; Feng, J.-K. *Polymer* **2004**, *45*, 7747–7757. (c) Cremer, J.; Briehn, C. A. *Chem. Mater.* **2007**, *19*, 4155–4165. (d) Zhang, W.-B.; Jin, W.-H.; Zhou, X.-H.; Pei, J. *Tetrahedron* **2007**, *63*, 2907–2914.

(31) (a) Marguet, S.; Germain, A.; Millie, P. *Chem. Phys.* **1996**, *208*, 351–373. (b) Minami, T.; Tretiak, S.; Chernyak, V.; Mukamel, S. *J. Lumin.* **2000**, *87*−*89*, 115–118.

(32) It should be noted that donor-acceptor substituted π-systems allow charge-transfer from the donor subunit to the acceptor subunit through cross-conjugated linkers such as meta-phenylene. See Yang, J.-S.; Liau, K.-L.; Li, C.-Y.; Chen, M.-Y. *J. Am. Chem. Soc.* **2007**, *129*, 13183–13192. and references cited therein. However, this type of electronic coupling does not conform to the concept of full π-conjugation, which corresponds to delocalized and overlapped HOMO and LUMO

(33) Wu, J.; Pisula, W.; Müllen, K. *Chem. Rev.* **2007**, *107*, 718–747.

(34) (a) Wadumethrige, S. H.; Rathore, R. *Org. Lett.* **2008**, *10*, 5139–5142. (b) Wong, W. W. H.; Jones, D. J.; Yan, C.; Watkins, S. E.; King, S.; Haque, S. A.; Wen, X.; Ghiggino, K. P.; Holmes, A. B. *Org. Lett.* **2009**, *11*, 975–978.

(35) Rao, C. N. R.; Sood, A. K.; Voggu, R.; Subrahmanyam, K. S. *J. Phys. Chem. Lett.* **2010**, *1*, 572–580.

(36) Wu, Y.-T.; Siegel, J. S. *Chem. Rev.* **2006**, *106*, 4843–4867.

(37) Guha, S.; Nakamoto, K. Coord. *Chem. Rev.* **2005**, *249*, 1111–1132.

(38) Pommerehne, J.; Vestweber, H.; Guss, W.; Mahrt, R. F.; Bässler, H.; Porsch, M.; Daub, J. *Adv. Mater.* **1995**, *7*, 551–554.

(39) Frisch, M. J.; et al. *Gaussian 09*, Revision A.02; Gaussian, Inc.: Wallingford CT, 2009.

(40) Dennington, R.; Keith, T.; Millam, J. *GaussView*, Version 5; Semichem Inc.: Shawnee Mission, KS, 2009.

(41) Lakowicz, J. R. *Principles of Fluorescence Spectroscopy*, 2nd ed.; Kluwer Academic/Plenum Publishers: New York, 1999.

(42) (a) He, G. S.; Tan, L.-S.; Zheng, Q.; Prasad, P. N. *Chem. Rev.* **2008**, *108*, 1245–1330. (b) Rumi, M; Barlow, S.; Wang, J.; Perry, J. W.; Marder, S. R. *Adv. Polym. Sci.* **2008**, *213*, 1–95.

(43) Tsao, H. N.; Müllen, K. *Chem. Soc. Rev.* **2010**, *39*, 2372–2386.